The Astronomical Journal, 153:178 (15pp), 2017 April https://doi.org/10.3847/1538-3881/aa5ffb

KELT-12b: A $P \sim 5$ day, Highly Inflated Hot Jupiter Transiting a Mildly Evolved Hot Star

Daniel J. Stevens[1], Karen A. Collins[2,3], B. Scott Gaudi[1], Thomas G. Beatty[4,5], Robert J. Siverd[6], Allyson Bieryla[7], Benjamin J. Fulton[8], Justin R. Crepp[9], Erica J. Gonzales[9,37], Carl T. Coker[1], Kaloyan Penev[10], Keivan G. Stassun[2,3], Eric L. N. Jensen[11], Andrew W. Howard[8], David W. Latham[7], Joseph E. Rodriguez[2,7], Roberto Zambelli[12], Valerio Bozza[13,14], Phillip A. Reed[15], Joao Gregorio[16], Lars A. Buchhave[17,18], Matthew T. Penny[1,38], Joshua Pepper[19], Perry Berlind[7], Sebastiano Calchi Novati[13,20], Michael L. Calkins[7], Giuseppe D'Ago[21,22], Jason D. Eastman[7], D. Bayliss[23], Knicole D. Colón[24,25], Ivan A. Curtis[26], D. L. DePoy[27,28], Gilbert A. Esquerdo[7], Andrew Gould[1], Michael D. Joner[29], John F. Kielkopf[30], Jonathan Labadie-Bartz[19], Michael B. Lund[2], Mark Manner[36], Jennifer L. Marshall[27,28], Kim K. McLeod[31], Thomas E. Oberst[32], Richard W. Pogge[1], Gaetano Scarpetta[13,21], Denise C. Stephens[29], Christopher Stockdale[33], T. G. Tan[34], Mark Trueblood[35], and Patricia Trueblood[35]

[1] Department of Astronomy, The Ohio State University, 140 W. 18th Ave., Columbus, OH 43210, USA
[2] Department of Physics and Astronomy, Vanderbilt University, Nashville, TN 37235, USA
[3] Department of Physics, Fisk University, Nashville, TN 37208, USA
[4] Department of Astronomy & Astrophysics, The Pennsylvania State University, 525 Davey Lab, University Park, PA 16802, USA
[5] Center for Exoplanets and Habitable Worlds, The Pennsylvania State University, 525 Davey Lab, University Park, PA 16802, USA
[6] Las Cumbres Observatory Global Telescope Network, 6740 Cortona Drive, Suite 102, Santa Barbara, CA 93117, USA
[7] Harvard-Smithsonian Center for Astrophysics, 60 Garden Street, Cambridge, MA 02138, USA
[8] Institute for Astronomy, University of Hawaii, 2680 Woodlawn Drive, Honolulu, HI 96822, USA
[9] Department of Physics, University of Notre Dame, 225 Nieuwland Science Hall, Notre Dame, IN 46556, USA
[10] Department of Astrophysical Sciences, Princeton University, Princeton, NJ 08544, USA
[11] Department of Physics and Astronomy, Swarthmore College, Swarthmore, PA 19081, USA
[12] Società Astronomica Lunae, Castelnuovo Magra I-19030, Italy
[13] Dipartimento di Fisica "E. R. Caianiello," Università di Salerno, Via Giovanni Paolo II 132, I-84084 Fisciano (SA), Italy
[14] Istituto Nazionale di Fisica Nucleare, Sezione di Napoli, I-80126 Napoli, Italy
[15] Department of Physical Sciences, Kutztown University, Kutztown, PA 19530, USA
[16] Atalaia Group & Crow-Observatory, Portalegre, Portugal
[17] Niels Bohr Institute, University of Copenhagen, Juliane Maries vej 30, DK-21S00 Copenhagen, Denmark
[18] Centre for Star and Planet Formation, Geological Museum, Øster Voldgade 5, DK-1350 Copenhagen, Denmark
[19] Department of Physics, Lehigh University, Bethlehem, PA, 18015, USA
[20] NASA Exoplanet Science Institute, MS 100-22, California Institute of Technology, 1200 E. California Boulevard, Pasadena, CA 91125, USA
[21] Istituto Internazionale per gli Alti Studi Scientifici (IIASS), Via G. Pellegrino 19, I-84019 Vietri sul Mare (SA), Italy
[22] INAF-Observatory of Capodimonte, Salita Moiariello, 16, I-80131, Naples, Italy
[23] Observatoire Astronomique de l'Université de Genève, 51 ch. des Maillettes, 1290 Versoix, Switzerland
[24] NASA Ames Research Center, M/S 244-30, Moffett Field, CA 94035, USA
[25] Bay Area Environmental Research Institute, 625 2nd Street, Ste 209, Petaluma, CA 94952, USA
[26] ICO, Adelaide, Australia
[27] George P. and Cynthia Woods Mitchell Institute for Fundamental Physics and Astronomy, Texas A&M University, College Station, TX 77843, USA
[28] Department of Physics & Astronomy, Texas A&M University, College Station, TX 77843-4242, USA
[29] Department of Physics and Astronomy, Brigham Young University, Provo, UT 84602, USA
[30] Department of Physics and Astronomy, University of Louisville, Louisville, KY 40292, USA
[31] Wellesley College, 106 Central Street, Wellesley, MA 02481, USA
[32] Department of Physics, Westminster College, New Wilmington, PA, 16172, USA
[33] Hazelwood Observatory, Victoria, Australia
[34] Perth Exoplanet Survey Telescope, Perth, Australia
[35] Winer Observatory, Sonoita, AZ 85637, USA
[36] Spot Observatory, Nashville, TN 37206 USA

Received 2016 August 16; revised 2017 January 28; accepted 2017 February 8; published 2017 March 24

Abstract

We announce the discovery of KELT-12b, a highly inflated Jupiter-mass planet transiting the mildly evolved, $V = 10.64$ host star TYC 2619-1057-1. We followed up the initial transit signal in the KELT-North survey data with precise ground-based photometry, high-resolution spectroscopy, precise radial velocity measurements, and high-resolution adaptive optics imaging. Our preferred best-fit model indicates that the host star has $T_{\rm eff} = 6279 \pm 51$ K, $\log g_\star = 3.89 \pm 0.05$, [Fe/H] $= 0.19^{+0.08}_{-0.09}$, $M_* = 1.59^{+0.07}_{-0.09}$ $M_\odot$, and $R_* = 2.37 \pm 0.17$ $R_\odot$. The planetary companion has $M_{\rm P} = 0.95 \pm 0.14$ $M_{\rm J}$, $R_{\rm P} = 1.78^{+0.17}_{-0.16}$ $R_{\rm J}$, $\log g_{\rm P} = 2.87^{+0.09}_{-0.10}$, and density $\rho_{\rm P} = 0.21^{+0.07}_{-0.05}$ g cm^{-3}, making it one of the most inflated giant planets known. Furthermore, for future follow-up, we report a high-precision time of inferior conjunction in $\rm BJD_{TDB}$ of 2,457,083.660459 $\pm$ 0.000894 and period of $P = 5.0316216 \pm 0.000032$ days. Despite the relatively large separation of $\sim$0.07 au implied by its $\sim$5.03-day

[37] NSF GRFP Fellow.
[38] Sagan Fellow.

orbital period, KELT-12b receives significant flux of $2.38^{+0.32}_{-0.29} \times 10^9$ erg s^{-1} cm^{-2} from its host. We compare the radii and insolations of transiting gas giant planets around hot ($T_{\rm eff} \geqslant 6250$ K) and cool stars, noting that the observed paucity of known transiting giants around hot stars with low insolation is likely due to selection effects. We underscore the significance of long-term ground-based monitoring of hot stars and space-based targeting of hot stars with the *Transiting Exoplanet Survey Satellite* to search for inflated gas giants in longer-period orbits.

Key words: planets and satellites: individual (KELT-12b) – stars: individual (KELT-12, TYC 2619-1057-1)

1. Introduction

The discovery of transiting exoplanets is generally partitioned into two regimes: giant planets on short-period orbits around bright stars and smaller planets around fainter stars. Ground-based transit surveys are most sensitive to the former, due to design and selection biases (Pepper et al. 2003; Gaudi 2005; Pepper & Gaudi 2005; Pont et al. 2006; Fressin et al. 2007; Beatty & Gaudi 2008), while space-based surveys such as *CoRoT* (Rouan et al. 1998) and *Kepler* (Borucki et al. 2010) specialize in the latter; the two-wheeled *Kepler* mission, *K2*, explores the intermediate regime (Howell et al. 2014).

In addition, the *Transiting Exoplanet Survey Satellite* (*TESS*; Ricker et al. 2015) will be sensitive to the same transiting systems to which the ground-based surveys are sensitive. However, many ground-based surveys—including the Hungarian-made Automated Telescope Network (HATNet; Bakos et al. 2004), the Kilodegree Extremely Little Telescope (KELT; Pepper et al. 2007, 2012), and SuperWASP (Pollacco et al. 2006), and their Northern Hemisphere components specifically—have been taking continuous observations of the night sky for approximately one decade. Thus, in the era of *TESS*, it may be possible to combine *TESS* data with those from ground-based surveys to discover and characterize longer-period giant planets than those that can be found with *TESS* data alone.

The KELT survey consists of two similar telescopes—one in Sonoita, Arizona (KELT-North; Pepper et al. 2007) and the other in Sutherland, South Africa (KELT-South; Pepper et al. 2012)—which are primarily sensitive to 1% flux changes in stars of V-band brightness $8 \leqslant V \leqslant 11$. KELT-North has found nine transiting substellar companions since starting in late 2006, while KELT-South has independently discovered four planets since starting operations in 2010, with a 14th planet found by both in an overlap survey field monitored by both telescopes (Zhou et al. 2016). KELT's continued monitoring of the same fields throughout its lifetime increases its sensitivity to long-duration and longer-period ($P \geqslant 5$ days) systems such as KELT-6b, which orbits its host once every ∼8 days (Collins et al. 2014).

Moreover, due to the KELT telescopes' sensitivity to giant planets around bright stars (which tend to be hot), the survey has discovered a few inflated planets: these include the giant planets KELT-4Ab (Eastman et al. 2016), KELT-6b (Collins et al. 2014), KELT-8b (Fulton et al. 2015), and KELT-11b (Pepper et al. 2016). Such companions are ideal targets for atmospheric characterization (e.g., Beatty et al. 2014), due to both their large radii and the brightness of their hosts; most planets with studied atmospheres have $V \leqslant 13$ (Sing et al. 2016; Seager & Deming 2010). They also provide clues about which environmental parameters (such as incident flux; Demory & Seager 2011) may drive exoplanetary radius inflation.

In this paper, we present the discovery and characterization of KELT-12b, an inflated hot Jupiter on a long (by ground-based transit standards), ∼5-day orbit around the hot star TYC 2619-1057-1, which is toward the end of its main-sequence lifetime. We place KELT-12b's extremely inflated radius in context, discuss radius inflation in hot Jupiters, and investigate its connection to incident flux and host star temperature.

2. Discovery and Follow-up Observations

Section 2.1 provides a summary of the pertinent KELT-North survey data, its reduction, and the light-curve processing. We detail the follow-up photometry in Section 2.2, radial velocity (RV) observations in Section 2.3, and adaptive optics (AO) imaging in Section 2.4.

2.1. KELT-North Photometry

KELT-12 is in KELT-North survey field 10, which is centered on ($\alpha = 17^{\rm h}30^{\rm m}43.4$, $\delta = +31°39'56\farcs2$; J2000). We monitored field 10 from 2007 January to 2013 June, collecting a total of 8150 observations. Our image reduction and light-curve processing are described in detail in Siverd et al. (2012), but we summarize the salient features here. In short, we reduced the raw survey data using a custom implementation of the ISIS image subtraction package (Alard & Lupton 1998; Alard 2000), combined with point-spread fitting photometry using DAOPHOT (Stetson 1987). To select likely dwarf and subgiant stars within the field for further analysis, we implemented a reduced proper-motion cut (Gould & Morgan 2003) based on the specific implementation of Collier Cameron et al. (2007); we used proper motions from the Tycho-2 catalog (Høg et al. 2000) and J and H magnitudes from the Two Micron All Sky Survey (2MASS; Cutri et al. 2003; Skrutskie et al. 2006).

In an update to the Siverd et al. (2012) procedure, we window-smoothed the stellar light curves with a 90-day window prior to applying both the Trend Filtering Algorithm (TFA; Kovács et al. 2005), to remove systematics common to nearby stars, and the Box Least-Squares algorithm (BLS; Kovács et al. 2002), to search the light curves for periodic boxcar-shaped transit signals. We used the TFA and BLS routines as implemented in the VARTOOLS package (Hartman 2012).

One of the candidates from field 10 that passed our selection criteria was TYC 2619-1057-1 at ($\alpha = 17^{\rm h}50^{\rm m}33\fs72$, $\delta = +36°34'12\farcs8$). The KELT-North discovery light curve exhibits a transit-like signal at a period of about 5.031 days with a depth of 4 mmag. The light curve contains 7497 observations—bad images (e.g., those with high cloud cover, high seeing, or significant moonlight contamination) were removed during the image reduction stage—and is shown in Figure 1. The broadband magnitudes and other stellar properties are listed in Table 1.

2.2. Follow-up Time-series Photometry

To improve the precision of the transit-derived parameters and to check against a false positive (e.g., blended eclipsing binary), we acquired several high-cadence, high-precision light curves from our global follow-up network of observers and small telescopes. We obtained a total of 15 partial and full

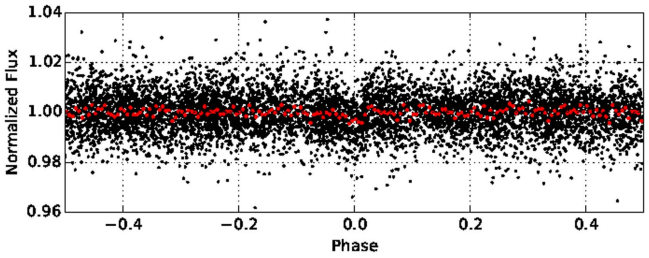

Figure 1. KELT-12b discovery light curve from the KELT-North telescope. The light curve contains 7498 observations spanning 6.3 yr. The light curve is phase-folded to the BLS-determined orbital period of 5.031450 days. The red filled circles show the same data binned at 1.2 hr intervals after phase-folding.

transits between 2014 August and 2015 August. The 5.03-day period and 5.8 hr duration made observing opportunities for full transits scarce. Figure 2 shows the follow-up light curves used in the global fit and analysis, and Table 2 gives a summary of the follow-up observations. Figure 3 shows all primary transit follow-up light curves from Figure 2 combined in 5-minute bins. We do not use this light curve for analysis, but we include it to illustrate the statistical power of the full suite of follow-up light curves.

We scheduled the follow-up observations using the `Tapir` software package (Jensen 2013) and reduced the follow-up photometric data with the `AstroImageJ` (AIJ) software package[39] (Collins & Kielkopf 2013; Collins et al. 2016). We also used AIJ to identify the best detrending parameters by calculating the Bayesian information criterion for different detrending parameter selections, and we included these parameters in the global fit (see Section 4.1).

2.2.1. Canela's Robotic Observatory (CROW)

On UT 2014 August 7, we observed one partial transit of KELT-12b at CROW in Portalegre, Portugal. We observed the ingress in the R_C filter with a 12-inch Schmidt–Cassegrain telescope and a KAF-3200E CCD, which gives a $30' \times 20'$ field of view and $0\farcs84\,\mathrm{pixel}^{-1}$ resolution.

2.2.2. Peter van de Kamp Observatory (PvdKO)

We obtained two partial transits and one full transit at PvdKO at Swarthmore College. We used the 0.6 m Ritchey–Chrétien optical (RCOS) telescope and Apogee U16M $4\mathrm{K} \times 4\mathrm{K}$ CCD, which give a $26' \times 26'$ field of view and $0\farcs76\,\mathrm{pixel}^{-1}$ resolution with 2×2 binning. We observed ingress in alternating g' and z' filters on UT 2014 September 27, and we observed a full transit in R on 2015 August 15.

2.2.3. Kutztown Observatory (Kutztown)

With the Kutztown University Observatory 0.6 m RCOS telescope, we observed most of a transit of KELT-12b in V and I bandpasses on UT 2014 September 27. This system employs a 3072×2048 CCD that achieves a $19\farcm5 \times 13\farcm0$ image at $0\farcs38\,\mathrm{pixel}^{-1}$.

2.2.4. KeplerCam

We used KeplerCam on the 1.2 m telescope at the Fred Lawrence Whipple Observatory (FLWO) to observe a partial i-band transit on UT 2015 April 06. KeplerCam has a single $4\mathrm{K} \times 4\mathrm{K}$ Fairchild CCD with $0\farcs366\,\mathrm{pixel}^{-1}$ and a field of view of $23\farcm1 \times 23\farcm1$.

2.2.5. Salerno University Observatory (Salerno)

We obtained an ingress in R on UT 2015 July 5, as well as a nearly full transit (sans egress) in B on UT 2015 July 10 from the Salerno University Observatory in Fisciano Salerno, Italy. The observing setup consists of a 14-inch Celestron C14 SCT and an SBIG ST2000XM 1600×1200 CCD, yielding a resolution of $0\farcs54\,\mathrm{pixel}^{-1}$.

2.2.6. Canis Mayor Observatory (ZRO)

From ZRO in Italy, we observed one nearly complete transit (missing only the ingress) on UT 2015 July 5, the full transit on 2015 July 10, and two separate ingresses on UT 2015 July 15 and UT 2015 July 20. All observations are V band. ZRO uses a 12-inch Meade LX 200 with an SBIG ST8XME 1530×1020 pixel CCD, which gives a resolution of $0\farcs92\,\mathrm{pixel}^{-1}$ over a $23\farcm5 \times 15\farcm7$ field of view.

2.2.7. Manner-Vanderbilt Ritchey–Chrétien (MVRC) Observatory

We observed one complete transit of KELT-12b on UT 2015 August 20 using the 0.6 m MVRC telescope at Mt. Lemmon Observatory in Arizona. The RCOS telescope is equipped with an SBIG STX $4\mathrm{K} \times 4\mathrm{K}$ camera, giving a $26' \times 26'$ field of view and $0\farcs39\,\mathrm{pixel}^{-1}$ resolution. The transit was observed in both the g' and i' bands by alternating filters from one exposure to the next.

2.3. Radial Velocity Observations

We conducted RV observations of KELT-12 to rule out false positives and to determine the RV orbit. We obtained data using both the Tillinghast Reflector Echelle Spectrograph[40] (TRES) on the 1.5 m Tillinghast Reflector at the FLWO on Mt. Hopkins, Arizona, and the Levy high-resolution optical spectrograph on the 2.4 m Automated Planet Finder[41] (APF) at Lick Observatory on Mt. Hamilton, California.

We observed KELT-12 with TRES over 5 months, from UT 2014 June 12 to UT 2014 November 17. We obtained 17 $R = 44{,}000$ spectra that were extracted following Buchhave et al. (2010). The first two observations, taken at quadrature, showed single-lined spectra (ruling out a double-lined eclipsing binary) and a low-velocity variation suggestive of a substellar companion. Additional high-precision observations were taken to obtain an RV orbit.

We then observed KELT-12 with APF over 2 months from UT 2015 May 28 to UT 2015 July 21. We obtained 21 $R = 100{,}000$ spectra that were extracted in a manner similar to that detailed in Section 3.2 of Fulton et al. (2015); for KELT-12, however, the iodine-free template was observed using the $1'' \times 3''$ slit, giving a resolution of ~33,000.

Initial fits to the RV data suggested a linear trend in addition to the periodic orbital motion. The TRES and APF data do not overlap in time, however: the first APF observation was taken after the UT 2014 November 17 TRES observation. To determine whether the linear trend is physical or due to a

[39] http://www.astro.louisville.edu/software/astroimagej/

[40] http://tdc-www.harvard.edu/instruments/tres

[41] http://www.ucolick.org/public/telescopes/apf.html

Table 1
KELT-12 Stellar Properties

Parameter	Description (Units)	Value	Source	Ref.
Names	⋯	TYC 2619-1057-1	SIMBAD	⋯
	⋯	GSC 02619-01057	SIMBAD	⋯
	⋯	2MASS J17503372+3634128	SIMBAD	⋯
α_{J2000}	⋯	17:50:33.719	Tycho-2	1
δ_{J2000}	⋯	+36:34:12.79	Tycho-2	1
FUV_{GALEX}	⋯	22.15 ± 0.970	*GALEX*	2
NUV_{GALEX}	⋯	15.31 ± 0.200	*GALEX*	2
B_T	⋯	11.328 ± 0.0550	Tycho-2	1
V_T	⋯	10.655 ± 0.0450	Tycho-2	1
V	⋯	10.644 ± 0.0440	TASS	3
I_C	⋯	9.998 ± 0.053	TASS	3
B	⋯	11.42 ± 0.190	APASS	4
V	⋯	10.59 ± 0.050	APASS	4
Sloan g'	⋯	11.10 ± 0.150	APASS	4
Sloan r'	⋯	10.44 ± 0.050	APASS	4
Sloan i'	⋯	10.31 ± 0.050	APASS	4
J	⋯	9.630 ± 0.030	2MASS	5
H	⋯	9.390 ± 0.030	2MASS	5
K	⋯	9.360 ± 0.030	2MASS	5
*WISE*1	⋯	12.01 ± 0.050	*WISE*	6
*WISE*2	⋯	12.67 ± 0.050	*WISE*	6
*WISE*3	⋯	14.60 ± 0.300	*WISE*	6
μ_α	Proper motion in RA (mas yr^{-1})	−0.40 ± 0.80	NOMAD	7
μ_δ	Proper motion in Dec. (mas yr^{-1})	−11.2 ± 0.70	NOMAD	7
γ_{abs}	Absolute systemic RV (km s^{-1})	−23.6 ± 0.1	This Paper[a]	⋯
d	Distance (pc)	360 ± 25	This Paper	⋯
Age	(Gyr)	2.2 ± 0.1	This Paper[b]	⋯
A_V	Visual extinction	0.1 ± 0.1	This Paper	⋯
(U[c], V, W)	Galactic space velocities (km s^{-1})	(U, V, W) = (16.1 ± 1.60, −12.1 ± 1.00, −8.1 ± 1.2)	This Paper[d]	⋯

Notes. Magnitudes are on the AB system. 2MASS and *WISE* uncertainties were increased to 0.03 and 0.05 mag, respectively, to account for systematic uncertainties.
References. (1) Høg et al. 2000; (2) Martin et al. 2005; (3) Richmond et al. 2000; (4) Henden et al. 2015; (5) Skrutskie et al. 2006; Cutri et al. 2003; (6) Wright et al. 2010; (7) Zacharias et al. 2004.
[a] The absolute RV uncertainty is due to the systematic uncertainties in the absolute velocities of the RV standard stars.
[b] The uncertainty does not include possible systematic errors in the adopted evolutionary tracks.
[c] We adopt a right-handed coordinate system such that positive U is toward the Galactic center.
[d] See Section 3.2.

systematic velocity offset between the TRES and APF data, we obtained four additional TRES observations from UT 2015 December 04 to UT 2016 February 14; thus, the APF data are bracketed in time by TRES observations. Table 3 lists the full set of RV observations from TRES and APF.

Our global fits presented in Section 4.2 all show that the RV linear trend persists at the ∼2.5σ level. Thus, the linear trend is not due to a systematic offset between the APF and TRES data, but it is not significant enough for us to claim a physical cause (e.g., a massive outer companion) for the linear trend. Long-term RV monitoring of the KELT-12 system will elucidate the origin of this trend.

Bisector spans (BSs) for both APF and TRES observations were calculated following the prescription of Buchhave et al. (2010) and are also listed in Table 3. We use the BSs as part of the false-positive analysis in Section 5, and we show them in Figure 4.

2.4. High-resolution Imaging

We obtained speckle imaging of KELT-12 from the Differential Speckle Survey Instrument (DSSI; Horch et al. 2009) on the WIYN 3.5 m telescope on UT 2015 October 25. DSSI is a speckle imaging camera that takes images in two bands simultaneously. Images are taken as sets of 1000 40 ms speckle frames and then later combined using the method detailed in Howell et al. (2011). The top two panels of Figure 5 show KELT-12 in narrow bands centered on 692 nm (R) and 880 nm (I); each image consists of multiple frame sets stacked into one reconstructed image. Observing conditions were worse than median for the WIYN site, with roughly 1″ seeing. No companions were detected down to a 5σ contrast limit of 3.31 mag in R and 2.78 mag in I. The bottom panels of Figure 5 show the R and I contrast curves. These curves are estimated using the method of Horch et al. (2011).

We also obtained AO imaging of KELT-12 from NIRC2 on Keck II in 2016 April. Figure 6 shows the K_s-band AO image and the contrast curve. With 0.″49 seeing and an airmass of 1.1, we achieved a 5σ contrast of approximately 9 mag at an angular separation of 1″; no companions were detected.

3. Host Star Properties

3.1. Properties from the Literature

Table 1 contains various measurements of KELT-12 collected from the literature or derived in this work. The literature information includes far-UV and near-UV fluxes from

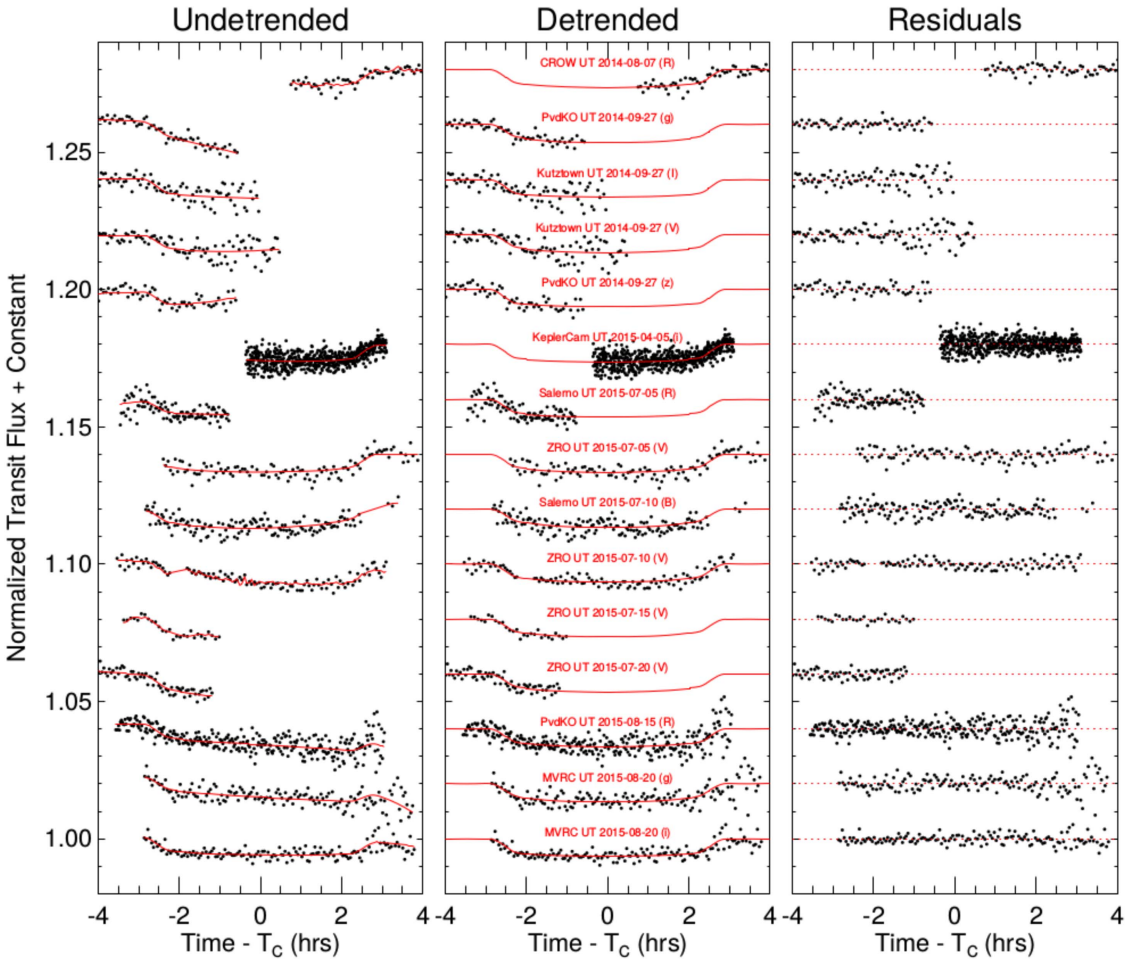

Figure 2. Undetrended (left) and detrended (middle) KELT-12b follow-up transit photometry (black filled circles) and best-fit transit model from the global fit described in Section 4.2 (red lines). Observatory abbreviations are given in Section 2.2. Light-curve residuals from the best-fit transit model are shown in the right panel.

Table 2
Follow-up Photometry of KELT-12

Date (UT)	Observatory	Filter	FOV	Pixel Scale	Exposure (s)	Detrending Parameters
2014 Aug 07	CROW	R_C	$30' \times 20'$	$0\farcs84$	150	Airmass, FWHM
2014 Sep 27	PvdKO	g'	$26' \times 26'$	$0\farcs76$	60	Airmass, time
2014 Sep 27	PvdKO	z'	$26' \times 26'$	$0\farcs76$	60	Airmass, time
2014 Sep 27	Kutztown	V	$19\farcm5 \times 13\farcm0$	$0\farcs38$	60	Airmass
2014 Sep 27	Kutztown	I	$19\farcm5 \times 13\farcm0$	$0\farcs38$	60	Airmass
2015 Apr 06	KeplerCam	i'	$23\farcm1 \times 23\farcm1$	$0\farcs37$	3	Airmass, time
2015 Jul 05	ZRO	V	$23\farcm5 \times 15\farcm7$	$0\farcs92$	200	Airmass
2015 Jul 05	Salerno	R	$14\farcm4 \times 10\farcm8$	$0\farcs54$	90	Airmass
2015 Jul 10	ZRO	V	$23\farcm5 \times 15\farcm7$	$0\farcs92$	200	Atm. loss[a], y-position[b]
2015 Jul 10	Salerno	B	$14\farcm4 \times 10\farcm8$	$0\farcs54$	120	Airmass
2015 Jul 15	ZRO	V	$23\farcm5 \times 15\farcm7$	$0\farcs92$	150	Airmass, FWHM
2015 Jul 20	ZRO	V	$23\farcm5 \times 15\farcm7$	$0\farcs92$	150	Airmass, time
2015 Aug 15	PvdKO	R_C	$26' \times 26'$	$0\farcs76$	60	Airmass, sky background
2015 Aug 20	MVRC	g'	$26' \times 26'$	$0\farcs39$	40	Airmass
2015 Aug 20	MVRC	i'	$26' \times 26'$	$0\farcs39$	80	Airmass

Notes.
[a] A representation of losses due to atmospheric changes. Calculated as airmass minus a scaled version of total comp star counts.
[b] The y-centroid pixel value.

GALEX (Martin et al. 2005); B_T and V_T fluxes from the Tycho-2 catalog (Høg et al. 2000); V and I_C from The Amateur Sky Survey (TASS; Richmond et al. 2000); B, V, and Sloan g', r', and i' fluxes from the AAVSO APASS catalog (Henden et al. 2015); near-infrared fluxes in the J, H, and K_S bands from the 2MASS Point Source Catalog (Cutri et al. 2003; Skrutskie

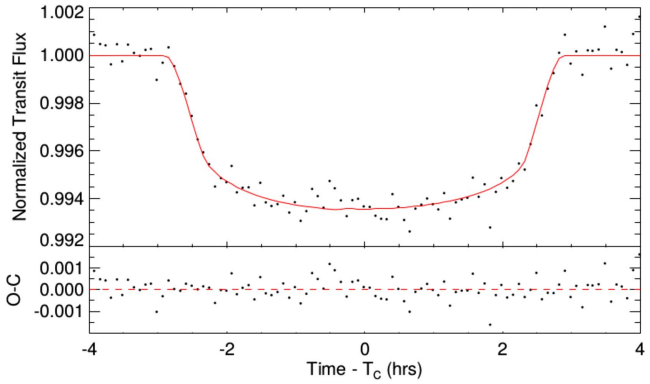

Figure 3. Top: multiband, composite KELT-12 follow-up light curve showing the 6 mmag depth reported by the adopted global fit. The black filled circles show the average of all follow-up light curves, combined in 5-minute bins. The combined best-fit models are shown as a solid red line. We did not use this composite light curve in our analysis, but we include it for illustrative purposes. Bottom: residuals between the 5-minute-binned, composite light curve shown above and the composite best-fit model.

et al. 2006); near- and mid-IR fluxes in three *WISE* passbands (Wright et al. 2010); and proper motions from the NOMAD catalog (Zacharias et al. 2004).

3.2. UVW Space Motion

We determine the motion of KELT-12 through the Galaxy to place it in one of the Galactic stellar populations. We adopt an absolute RV of -23.55 ± 0.1 km s^{-1} by calculating the error-weighted mean of the TRES and APF mean absolute RVs. We list the individual absolute RVs in Table 3; the uncertainty on the RVs comes from the systematic uncertainties in the absolute RVs of the RV standard stars. We calculate *U, V,* and *W* space velocities by combining the adopted absolute RV with proper motions from NOMAD (Zacharias et al. 2004) and the distance that we estimate from fitting the spectral energy distribution (SED; Section 3.3). We adopt the Coşkunoğlu et al. (2011) solar velocity with respect to the local standard of rest.

For KELT-12, $(U, V, W) = (16.1 \pm 1.6, -12.1 \pm 1.0, -8.1 \pm 1.2)$—all in units of km s^{-1}—where positive U points toward the Galactic center. We find a 99.3% probability that KELT-12 is a thin-disk star, according to Bensby et al. (2003).

3.3. SED Analysis

Using the broadband literature photometry listed in Table 1 and in Section 3.1, we create an empirical SED of KELT-12. We fit this SED to NextGen stellar atmosphere models from Hauschildt et al. (1999) by fixing the values of $T_{\rm eff}$, $\log g_\star$, and [Fe/H] to the values that we infer from the global light curve and RV fit and the spectroscopic data; we list these parameters in Table 4. Next, we find the values of the visual extinction A_V and distance d that minimize the χ^2 of the fit. Figure 7 shows the best-fit model SED and the literature photometry for KELT-12. The best-fit model yields a reduced χ^2 of 1.99 for 12 degrees of freedom. This reduced χ^2 exceeds unity, suggesting that the photometric uncertainties are underestimated. We find $A_V = 0.1 \pm 0.1$ and $d = 360 \pm 25$ pc.

Because we do not account for uncertainties in the values of $T_{\rm eff}$, $\log g_\star$, and [Fe/H] that we use to derive the model SED, we caution that the quoted statistical uncertainties on A_V and d are likely to be underestimated as well. Moreover, choosing a different stellar model atmosphere would yield somewhat different SEDs, which may then produce different extinctions and distances.

Table 3
Radial Velocity and Bisector Span Variation Measurements of KELT-12

BJD$_{\rm TDB}$	Rel RV[a]	Rel $\sigma_{\rm RV}$[b]	BS[c]	$\sigma_{\rm BS}$[d]	Source
2,456,820.716376	−71.36	45.54	31.4	22.4	TRES
2,456,858.681075	−146.54	25.68	−13.9	22.7	TRES
2,456,902.667051	−76.83	27.45	4.3	11.4	TRES
2,456,903.649365	−104.45	23.31	−15.2	12.8	TRES
2,456,931.603340	58.18	24.40	−16.2	13.2	TRES
2,456,942.582475	−31.91	36.05	−5.4	17.4	TRES
2,456,961.605609	10.19	27.28	14.3	12.5	TRES
2,456,970.587814	−28.87	27.59	−6.6	14.5	TRES
2,456,971.626563	98.73	23.83	−25.7	13.2	TRES
2,456,972.570012	0.00	21.65	−22.7	8.7	TRES
2,456,973.591941	−59.52	46.67	23.3	18.6	TRES
2,456,974.572029	−85.15	33.93	8.1	11.7	TRES
2,456,975.573986	−14.03	27.10	13.3	9.1	TRES
2,456,976.619038	−5.85	86.65	42.8	31.1	TRES
2,456,977.570913	7.64	29.79	−27.8	19.7	TRES
2,456,978.579390	−63.94	43.72	1.1	15.4	TRES
2,457,170.875234	−71.552	20.236	−27.53	32.49	APF
2,457,176.874662	−58.679	29.458	120.88	27.73	APF
2,457,176.905670	−81.028	26.790	152.24	47.21	APF
2,457,179.907450	−48.511	18.798	22.04	23.69	APF
2,457,181.812386	−23.575	20.735	−106.82	45.24	APF
2,457,185.791278	−8.415	25.342	165.72	134.76	APF
2,457,185.876904	−5.665	23.185	−68.72	34.65	APF
2,457,188.903940	35.698	19.091	−65.81	53.58	APF
2,457,189.883791	−41.047	21.227	−94.96	73.25	APF
2,457,191.909406	4.362	18.508	71.93	47.05	APF
2,457,193.889717	47.605	23.534	54.79	64.07	APF
2,457,195.864283	−124.077	18.274	25.99	30.52	APF
2,457,196.878076	9.207	19.350	−57.30	29.94	APF
2,457,202.756011	89.352	25.827	−108.97	45.76	APF
2,457,211.817088	43.054	20.238	−113.89	129.68	APF
2,457,217.806699	145.956	21.300	−3.76	55.51	APF
2,457,218.800069	120.374	17.939	50.35	48.54	APF
2,457,220.714713	−66.971	19.395	52.30	30.09	APF
2,457,221.717931	−47.358	21.042	13.77	44.14	APF
2,457,222.722571	60.293	22.267	40.62	44.60	APF
2,457,224.723782	17.005	20.679	−24.84	45.09	APF
2,457,360.571424	−6.17	60.99	−1.3	18.9	TRES
2,457,416.034345	−78.71	28.90	−0.7	14.1	TRES
2,457,428.044913	126.02	21.65	−22.0	22.0	TRES
2,457,433.029939	−82.95	21.93	19.0	11.8	TRES

Notes. The relative RV values reported are on the native system for each instrument and cannot be directly compared to values from a different instrument. The bisector spans (BS) from the TRES spectra are computed as described in the text.
[a] Relative RVs (m s^{-1}).
[b] Unrescaled relative RV errors (m s^{-1}).
[c] Spectral line bisector spans (m s^{-1}).
[d] Spectral line bisector span errors (m s^{-1}).

3.4. Spectroscopic Analysis

We derive KELT-12's stellar properties from both the APF and TRES spectra. To analyze the APF spectra, we use SpecMatch (Petigura 2015). This analysis yields $T_{\rm eff} = 6229 \pm 60$ K, $\log g_\star = 4.1 \pm 0.08$, [Fe/H] $= 0.22 \pm 0.04$, and $v \sin I_\star = 10.59 \pm 0.43$ km s^{-1}.

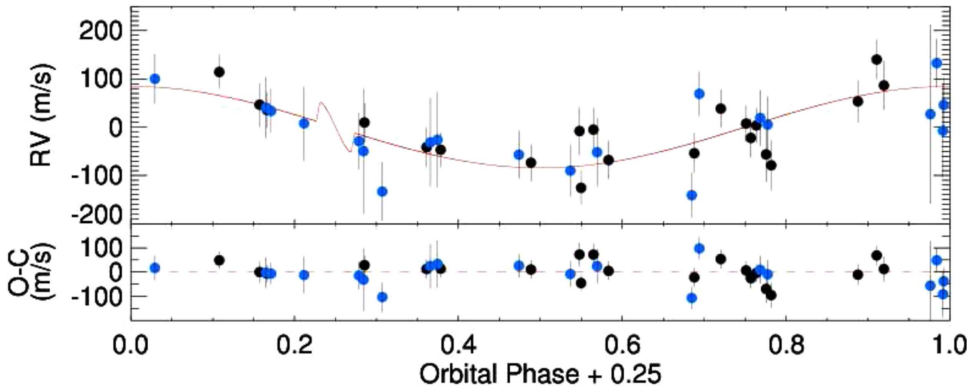

Figure 4. Top: KELT-12 relative radial velocity measurements from APF (black filled circles) and TRES (blue filled circles) phase-folded to the best-fit orbital model (red line; see Section 4.2). The Rossiter–McLaughlin effect at phase 0.25 assumes that the projected spin–orbit alignment $\lambda = 0$. Bottom: RV residuals from the best-fit model.

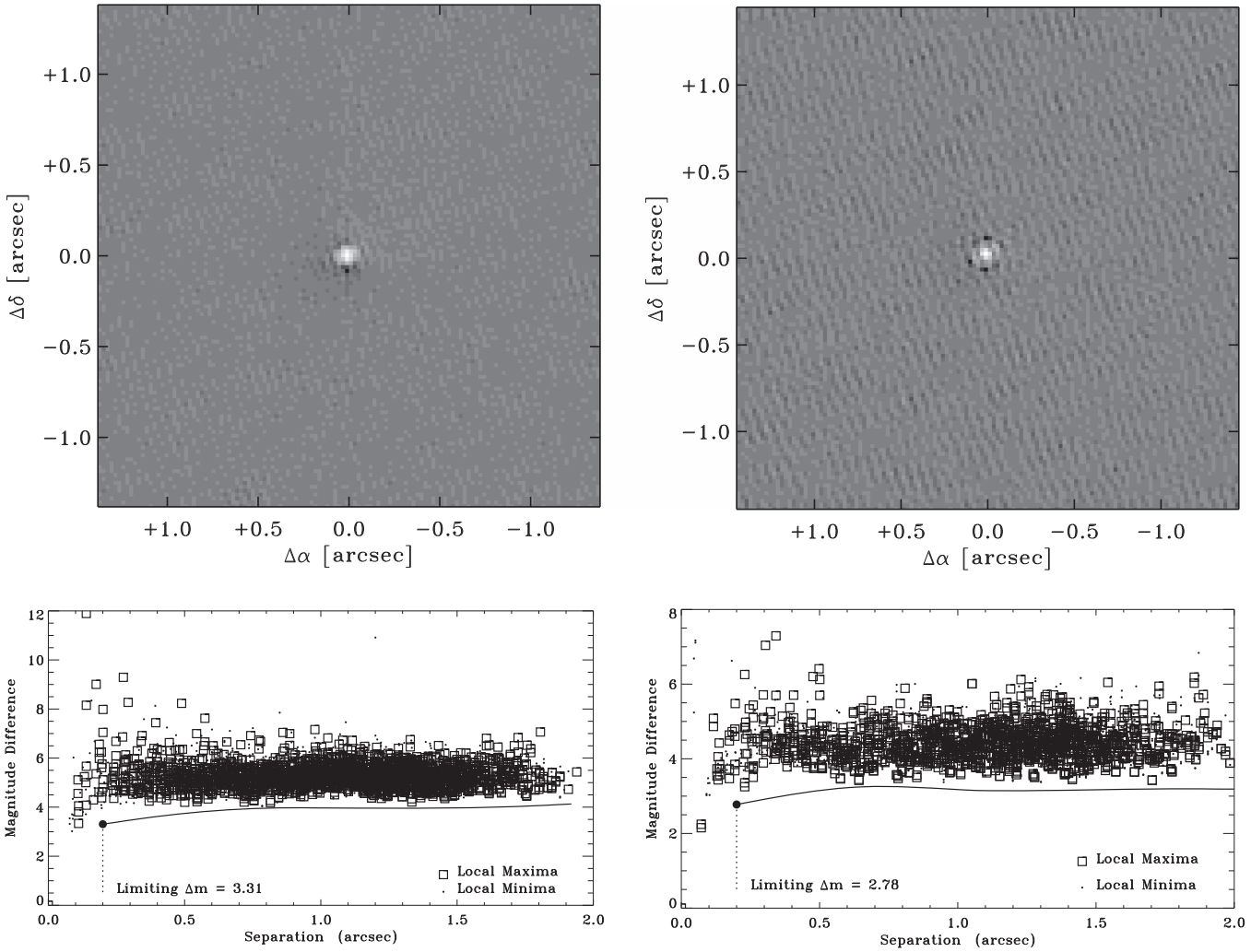

Figure 5. Stacked DSSI images (top) and contrast curves (bottom) of KELT-12 in R (left) and I (right). Each square point in the bottom two panels represents the magnitude difference between a given pixel in the image and the central star. No statistically significant companions were detected down to a 5σ magnitude contrast of $\Delta R = 3.31$ and $\Delta I = 2.78$ at an angular separation of $0\farcs2$.

To analyze the TRES spectra, we use the Spectral Parameter Classification (SPC) procedure, version 2.2 (Buchhave et al. 2012). We ran SPC initially with $T_{\rm eff}$, $\log g_\star$, [m/H], and $v \sin I_\star$ as free parameters. We took the error-weighted mean value for each stellar parameter and adopted the mean error for each parameter. From this initial run, we found that $T_{\rm eff} = 6355 \pm 51$ K, $\log g_\star = 4.16 \pm 0.09$, [m/H] $= 0.27 \pm 0.05$, and $v \sin I_\star = 12.1 \pm 0.2$ km s^{-1}. The surface gravity and metallicity agree with the APF SpecMatch value within 1σ; of note, $T_{\rm eff}$ differs by 2.5σ. Additionally, an initial analysis of the transit data with stellar models and with empirical relations using the APF $T_{\rm eff}$ and [Fe/H] values as priors resulted in

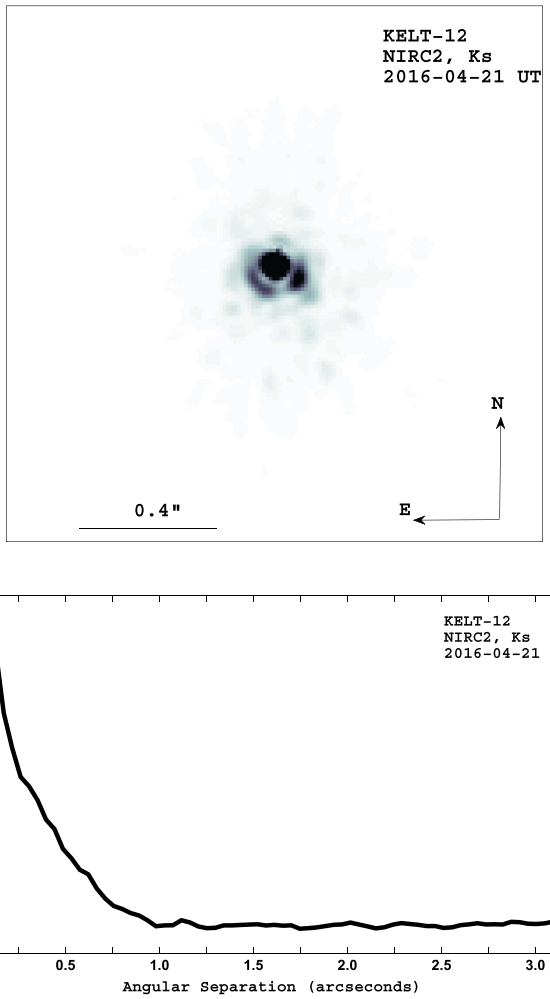

Figure 6. AO image of KELT-12 taken with NIRC2 on the Keck II telescope (top) and the 5σ contrast curve (bottom). No statistically significant companions were detected down to a 5σ magnitude contrast of $\Delta K_S = 9$ at $1''$ separation.

$\log g_\star = 3.9 \pm 0.08$, inconsistent with both APF and TRES values at $\geqslant 2.5\sigma$.

Because the gravity from the transit data and stellar models is expected to be more accurate than the spectroscopic gravities, we reran SPC on the TRES data with the surface gravity fixed at $\log g_\star = 3.9$, giving us $T_{\rm eff} = 6281 \pm 59$ K, $\log g_\star = 3.90 \pm 0.00$, $[{\rm m/H}] = 0.21 \pm 0.07$, and $v \sin I_\star = 12.2 \pm 0.2$ km s^{-1} and bringing $T_{\rm eff}$, $\log g_\star$, and metallicity into agreement ($\sim 1\sigma$) with the APF SpecMatch values. We impose these $T_{\rm eff}$, [m/H], and $v \sin I_\star$ values and uncertainties as Gaussian priors for the final analysis in Section 4.2.

4. Planetary Characterization

To determine the physical and observable properties of the KELT-12 system, we perform a global fit of the photometric and spectroscopic data using a modified version of the IDL exoplanet fitting tool EXOFAST (Eastman et al. 2013). In short, we run simultaneous Markov chain Monte Carlo analyses on the RV data and follow-up photometry to determine the posterior probability distribution of each parameter; the technique is described in detail in Siverd et al. (2012). EXOFAST constrains the stellar mass and radius by using either the Yonsei–Yale (YY) stellar evolution models

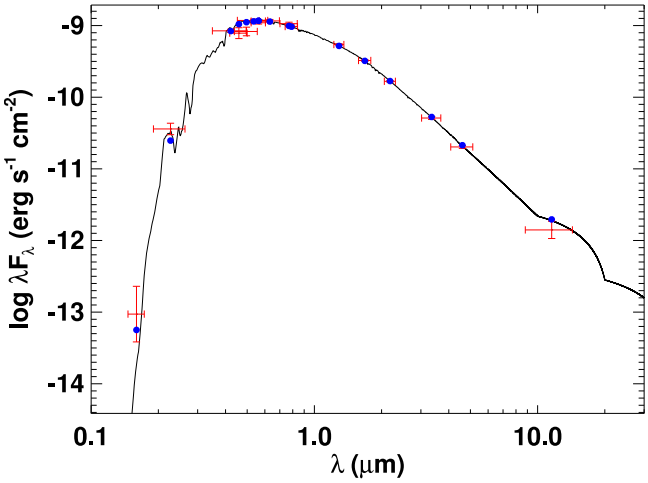

Figure 7. Best-fit SED for KELT-12 using UV through mid-IR flux measurements. The intersection of the red error bars indicates KELT-12 flux measurements listed in Table 1. The vertical error bars are the 1σ photometric uncertainties, whereas the horizontal error bars are the passbands' effective widths. The solid curve is the best-fit theoretical SED from the NextGen models of Hauschildt et al. (1999), assuming stellar parameters $T_{\rm eff}$, $\log g_\star$, and [Fe/H] fixed at the fiducial global fit values as listed in Table 4; we allow $A_{\rm V}$ and d to vary. The blue dots are the predicted passband-integrated fluxes of the best-fit theoretical SED that correspond to our observed photometric bands.

(Demarque et al. 2004) or the empirical relations of Torres et al. (2010) (hereafter "the Torres relations"). We include the raw follow-up photometry and the relevant detrending parameters (see Section 4.1) in the fits. We set a prior on the orbital period $P = 5.031623 \pm 0.00003$ days from analysis of the KELT-North discovery light curve and the follow-up photometry.

4.1. Light-curve Detrending

Owing to the KELT-12 system's nearly 6 hr transit duration, our analysis relies extensively on partial transits. As a result of this and the shallow, $\sim$6 mmag transit depth, the shape of the transit and the inferred transit parameters can thus be heavily influenced by our choice of detrending parameters. As described in Collins et al. (2014), we use AIJ to determine the detrending parameters that best improve the individual light-curve fits, as including all possible detrending parameters for all light curves in the EXOFAST global fit would be prohibitively expensive from a computational point of view. We list the included detrending parameters for each fitted data set in Table 2.

4.2. Global Fit

To determine the prior values of $T_{\rm eff}$, [Fe/H], and $v \sin I_\star$ that we imposed on the final global fits, we performed an iterative SPC analysis as described in Section 3.4 and adopted the final TRES SPC values for $T_{\rm eff}$, [Fe/H], and $v \sin I_\star$ as spectroscopic priors.

Given our lack of full transits with out-of-transit baselines, we find that the MCMC fits fail to converge without imposing priors on the transit timing variations (TTVs) of each observation and their out-of-transit flux baselines, F_0. To avoid unduly biasing the MCMC toward any values used in a Gaussian prior, we adopt uniform priors on the TTVs (centered on 0 days with a 0.03-day half-width) and F_0 (centered on the normalized value of 1 with a 1% half-width). We inspect the

Table 4
Median Values and 68% Confidence Interval for the Physical and Orbital Parameters of the KELT-12 System

Parameter	Units	Adopted Value (YY circular; $e = 0$ fixed)	Value (YY eccentric)	Value (Torres circular; $e = 0$ fixed)	Value (Torres eccentric)
Stellar parameters:					
M_*	Mass ($M_\odot$)	$1.591^{+0.070}_{-0.093}$	1.61 ± 0.11	$1.517^{+0.081}_{-0.078}$	$1.533^{+0.10}_{-0.094}$
R_*	Radius ($R_\odot$)	2.37 ± 0.17	$2.46^{+0.37}_{-0.28}$	$2.33^{+0.16}_{-0.17}$	$2.38^{+0.31}_{-0.25}$
L_*	Luminosity ($L_\odot$)	$7.8^{+1.2}_{-1.1}$	$8.5^{+2.8}_{-1.9}$	$7.6^{+1.2}_{-1.1}$	$7.9^{+2.2}_{-1.6}$
ρ_*	Density (cgs)	$0.168^{+0.035}_{-0.028}$	$0.152^{+0.056}_{-0.047}$	$0.170^{+0.036}_{-0.027}$	$0.160^{+0.055}_{-0.044}$
$\log g_*$	Surface gravity (cgs)	$3.889^{+0.051}_{-0.050}$	$3.862^{+0.084}_{-0.10}$	$3.886^{+0.052}_{-0.047}$	$3.870^{+0.080}_{-0.086}$
$T_{\rm eff}$	Effective temperature (K)	6279 ± 51	6280 ± 50	6285 ± 49	6285 ± 49
[Fe/H]	Metallicity	$0.190^{+0.084}_{-0.085}$	$0.193^{+0.082}_{-0.083}$	$0.203^{+0.078}_{-0.079}$	$0.203^{+0.079}_{-0.078}$
Planetary parameters:					
e	Eccentricity	⋯	$0.083^{+0.090}_{-0.058}$	⋯	$0.076^{+0.081}_{-0.053}$
ω_*	Argument of periastron (degrees)	⋯	52^{+59}_{-94}	⋯	42^{+69}_{-94}
P	Period (days)	$5.031623^{+0.000032}_{-0.000031}$	5.031623 ± 0.000032	5.031623 ± 0.000032	5.031623 ± 0.000031
a	Semimajor axis (au)	$0.06708^{+0.00097}_{-0.0013}$	0.0674 ± 0.0015	$0.0660^{+0.0012}_{-0.0011}$	$0.0663^{+0.0015}_{-0.0014}$
M_P	Mass ($M_{\rm J}$)	0.95 ± 0.14	0.96 ± 0.15	$0.93^{+0.14}_{-0.13}$	0.93 ± 0.15
R_P	Radius ($R_{\rm J}$)	$1.78^{+0.17}_{-0.16}$	$1.86^{+0.30}_{-0.24}$	1.74 ± 0.16	$1.79^{+0.26}_{-0.22}$
ρ_P	Density (cgs)	$0.209^{+0.071}_{-0.053}$	$0.184^{+0.095}_{-0.067}$	$0.215^{+0.073}_{-0.053}$	$0.201^{+0.095}_{-0.067}$
$\log g_P$	Surface gravity	$2.872^{+0.092}_{-0.096}$	$2.83^{+0.13}_{-0.14}$	$2.876^{+0.092}_{-0.094}$	$2.86^{+0.12}_{-0.13}$
T_{eq}	Equilibrium temperature (K)	1800 ± 57	1831^{+120}_{-94}	1798^{+55}_{-58}	1816^{+100}_{-89}
Θ	Safronov number	$0.0453^{+0.0079}_{-0.0073}$	$0.0429^{+0.0098}_{-0.0087}$	$0.0462^{+0.0081}_{-0.0074}$	$0.0447^{+0.0097}_{-0.0087}$
$\langle F \rangle$	Incident flux (10^9 erg s^{-1} cm^{-2})	$2.38^{+0.32}_{-0.29}$	$2.54^{+0.65}_{-0.48}$	$2.37^{+0.31}_{-0.29}$	$2.46^{+0.56}_{-0.45}$
RV parameters:					
T_C	Time of inferior conjunction (BJD$_{\rm TDB}$)	$2457083.66031 \pm 0.00090$	$2457083.66030^{+0.00091}_{-0.00090}$	$2457083.66031^{+0.00091}_{-0.00090}$	$2457083.66031 \pm 0.00090$
T_P	Time of periastron (BJD$_{\rm TDB}$)	⋯	$2457083.25^{+0.68}_{-1.3}$	⋯	$2457083.13^{+0.83}_{-1.3}$
K	RV semi-amplitude (m s^{-1})	82 ± 12	82 ± 13	82 ± 12	82 ± 13
$M_P \sin i$	Minimum mass ($M_{\rm J}$)	0.95 ± 0.14	0.95 ± 0.15	0.92 ± 0.13	$0.92^{+0.15}_{-0.14}$
M_P/M_*	Mass ratio	0.000576 ± 0.000081	$0.000568^{+0.000089}_{-0.000088}$	0.000583 ± 0.000082	0.000578 ± 0.000089
u	RM linear limb darkening	$0.6092^{+0.0061}_{-0.0055}$	$0.6092^{+0.0062}_{-0.0055}$	$0.6093^{+0.0061}_{-0.0056}$	$0.6093^{+0.0061}_{-0.0055}$
$\gamma_{\rm APF}$	(m s^{-1})	-8 ± 12	-8 ± 13	-8 ± 12	-8 ± 13
$\gamma_{\rm TRES}$	(m s^{-1})	-16 ± 14	-16 ± 15	-16 ± 14	-16 ± 15
$\dot{\gamma}$	RV slope (m s^{-1} day^{-1})	0.160 ± 0.065	0.168 ± 0.072	$0.160^{+0.065}_{-0.066}$	0.169 ± 0.072
$e \cos \omega_\star$	⋯	⋯	$0.026^{+0.060}_{-0.041}$	⋯	$0.025^{+0.059}_{-0.039}$
$e \sin \omega_\star$	⋯	⋯	$0.022^{+0.12}_{-0.061}$	⋯	$0.012^{+0.098}_{-0.059}$
$f(m1, m2)$	Mass function ($M_{\rm J}$)	$0.00000031^{+0.00000015}_{-0.00000011}$	$0.00000030^{+0.00000016}_{-0.00000012}$	$0.00000031^{+0.00000015}_{-0.00000011}$	$0.00000031^{+0.00000016}_{-0.00000012}$
Primary transit parameters:					
R_P/R_*	Radius of the planet in stellar radii	$0.0772^{+0.0019}_{-0.0018}$	0.0772 ± 0.0019	0.0771 ± 0.0018	$0.0771^{+0.0018}_{-0.0019}$
a/R_*	Semimajor axis in stellar radii	$6.08^{+0.40}_{-0.36}$	$5.88^{+0.65}_{-0.68}$	$6.11^{+0.40}_{-0.34}$	$5.99^{+0.62}_{-0.60}$
i	Inclination (deg)	$84.47^{+1.1}_{-0.95}$	$84.1^{+1.5}_{-1.9}$	$84.54^{+1.1}_{-0.91}$	$84.3^{+1.4}_{-1.6}$
b	Impact parameter	$0.586^{+0.060}_{-0.082}$	$0.587^{+0.059}_{-0.082}$	$0.581^{+0.059}_{-0.084}$	$0.580^{+0.060}_{-0.087}$
δ	Transit depth	$0.00596^{+0.00029}_{-0.00028}$	$0.00596^{+0.00029}_{-0.00028}$	0.00594 ± 0.00028	$0.00594^{+0.00029}_{-0.00028}$
T_0	Time of inferior conjunction[b] (BJD$_{\rm TDB}$)	2457083.660459± 0.000894	2457083.660687± 0.000912	2457083.660464± 0.000888	2457088.692293± 0.000882
$P_{\rm Transit}$	Period[b] (days)	5.0316216 ± 0.000032	5.0316216 ± 0.000032	5.0316213 ± 0.000031	5.0316216 ± 0.000032
$T_{\rm FWHM}$	FWHM duration (days)	$0.2146^{+0.0024}_{-0.0023}$	$0.2146^{+0.0025}_{-0.0024}$	$0.2146^{+0.0024}_{-0.0023}$	$0.2146^{+0.0024}_{-0.0023}$

Table 4
(Continued)

Parameter	Units	Adopted Value (YY circular; $e = 0$ fixed)	Value (YY eccentric)	Value (Torres circular; $e = 0$ fixed)	Value (Torres eccentric)
τ	Ingress/egress duration (days)	$0.0255^{+0.0039}_{-0.0035}$	$0.0256^{+0.0038}_{-0.0036}$	$0.0253^{+0.0037}_{-0.0035}$	$0.0252^{+0.0038}_{-0.0036}$
T_{14}	Total duration (days)	$0.2401^{+0.0049}_{-0.0043}$	$0.2402^{+0.0049}_{-0.0044}$	$0.2398^{+0.0047}_{-0.0042}$	$0.2397^{+0.0047}_{-0.0043}$
P_T	A priori nongrazing transit probability	$0.1517^{+0.0093}_{-0.0091}$	$0.161^{+0.045}_{-0.023}$	$0.1512^{+0.0088}_{-0.0091}$	$0.157^{+0.035}_{-0.021}$
$P_{T,G}$	A priori transit probability	0.177 ± 0.011	$0.188^{+0.052}_{-0.027}$	0.176 ± 0.011	$0.183^{+0.041}_{-0.025}$
u_{1B}	Linear limb darkening	$0.558^{+0.013}_{-0.012}$	$0.558^{+0.013}_{-0.012}$	$0.558^{+0.013}_{-0.012}$	0.558 ± 0.012
u_{2B}	Quadratic limb darkening	$0.2272^{+0.0076}_{-0.0083}$	$0.2265^{+0.0078}_{-0.0084}$	$0.2274^{+0.0076}_{-0.0081}$	$0.2270^{+0.0076}_{-0.0081}$
u_{1I}	Linear limb darkening	$0.2139^{+0.0062}_{-0.0055}$	$0.2131^{+0.0064}_{-0.0059}$	$0.2134^{+0.0061}_{-0.0056}$	$0.2130^{+0.0063}_{-0.0059}$
u_{2I}	Quadratic limb darkening	$0.3164^{+0.0037}_{-0.0034}$	$0.3171^{+0.0038}_{-0.0036}$	$0.3170^{+0.0035}_{-0.0033}$	$0.3174^{+0.0037}_{-0.0035}$
u_{1R}	Linear limb darkening	$0.2901^{+0.0071}_{-0.0061}$	$0.2896^{+0.0071}_{-0.0063}$	$0.2898^{+0.0070}_{-0.0062}$	$0.2894^{+0.0070}_{-0.0063}$
u_{2R}	Quadratic limb darkening	0.3226 ± 0.0031	0.3230 ± 0.0031	0.3231 ± 0.0029	0.3233 ± 0.0030
$u_{1Sloang}$	Linear limb darkening	$0.4845^{+0.011}_{-0.0096}$	$0.4850^{+0.011}_{-0.0097}$	$0.4845^{+0.011}_{-0.0097}$	$0.4848^{+0.010}_{-0.0096}$
$u_{2Sloang}$	Quadratic limb darkening	$0.2654^{+0.0051}_{-0.0058}$	$0.2649^{+0.0052}_{-0.0058}$	$0.2655^{+0.0051}_{-0.0057}$	$0.2653^{+0.0051}_{-0.0056}$
$u_{1Sloani}$	Linear limb darkening	$0.2330^{+0.0063}_{-0.0056}$	$0.2322^{+0.0065}_{-0.0059}$	$0.2325^{+0.0063}_{-0.0056}$	$0.2321^{+0.0064}_{-0.0059}$
$u_{2Sloani}$	Quadratic limb darkening	$0.3180^{+0.0036}_{-0.0035}$	$0.3186^{+0.0037}_{-0.0036}$	$0.3186^{+0.0034}_{-0.0033}$	$0.3190^{+0.0036}_{-0.0035}$
$u_{1Sloanz}$	Linear limb darkening	$0.1818^{+0.0056}_{-0.0051}$	$0.1812^{+0.0057}_{-0.0053}$	$0.1813^{+0.0055}_{-0.0051}$	$0.1810^{+0.0056}_{-0.0053}$
$u_{2Sloanz}$	Quadratic limb darkening	$0.3083^{+0.0035}_{-0.0031}$	$0.3089^{+0.0036}_{-0.0033}$	$0.3089^{+0.0033}_{-0.0030}$	$0.3093^{+0.0034}_{-0.0032}$
u_{1V}	Linear limb darkening	$0.3821^{+0.0083}_{-0.0072}$	$0.3820^{+0.0083}_{-0.0072}$	$0.3820^{+0.0082}_{-0.0073}$	$0.3819^{+0.0082}_{-0.0072}$
u_{2V}	Quadratic limb darkening	$0.3044^{+0.0029}_{-0.0035}$	$0.3044^{+0.0028}_{-0.0034}$	$0.3047^{+0.0028}_{-0.0033}$	$0.3046^{+0.0028}_{-0.0032}$
Secondary eclipse parameters:					
T_S	Time of eclipse (BJD_{TDB})	$2457081.14450 \pm 0.00090$	$2457081.23^{+0.19}_{-0.13}$	$2457081.14449 \pm 0.00091$	$2457081.22^{+0.19}_{-0.12}$
b_S	Impact parameter	⋯	$0.62^{+0.17}_{-0.13}$	⋯	$0.60^{+0.13}_{-0.12}$
$T_{S,\mathrm{FWHM}}$	FWHM duration (days)	⋯	$0.214^{+0.011}_{-0.022}$	⋯	$0.214^{+0.011}_{-0.018}$
τ_S	Ingress/egress duration (days)	⋯	$0.0275^{+0.016}_{-0.0068}$	⋯	$0.0263^{+0.011}_{-0.0060}$
$T_{S,14}$	Total duration (days)	⋯	$0.244^{+0.015}_{-0.022}$	⋯	$0.243^{+0.015}_{-0.021}$
P_S	A priori nongrazing eclipse probability	⋯	$0.1534^{+0.0093}_{-0.0095}$	⋯	$0.1524^{+0.0092}_{-0.0095}$
$P_{S,G}$	A priori eclipse probability	⋯	$0.179^{+0.011}_{-0.012}$ ⋯	$0.178^{+0.011}_{-0.012}$	

Notes.
[a] Relative RVs (m s^{-1}).
[b] From the best-fit linear ephemeris.

TTV and F_0 posterior probability density functions for each light curve to verify that the likelihood is essentially zero at the limiting values of our priors. We therefore believe that our use of priors is not biasing the final values inferred by our MCMC, but rather is serving the purpose of preventing these poorly behaved parameters from falling into multiple local minima.

We ran the global fits using either the YY isochrones or the Torres relations, and we either forced circular orbits or allowed for eccentric orbits; permutation of these choices yielded four global fits. In all four fits, we allowed for a nonzero RV slope. As described in Eastman et al. (2013), the MCMC routine proposes jumps in the following parameters: the systemic RVs γ_{APF} and γ_{TRES}, the RV slope $\dot{\gamma}$, T_C, $\log P$, $\sqrt{e}\cos\omega_*$, $\sqrt{e}\sin\omega_*$, $\log K$, $\cos i$, R_P/R_*, $\log a/R_*$, $\log g_\star$, T_{eff}, [Fe/H], F_0, and the detrending parameters for each light curve. The quadratic limb-darkening parameters u_1 and u_2 are calculated from T_{eff}, $\log g_\star$, and [Fe/H] at each step.

Table 4 list the best-fit parameters and their 68% confidence intervals for the four cases. While the two eccentric fits report eccentricities that are formally inconsistent with zero at the $\sim 1.45\sigma$ level, eccentricity measurements are biased to artificially large values, due to the hard boundary at 0, so a significance of $\geqslant 2.5\sigma$ is generally required to claim an eccentric orbit (Lucy & Sweeney 1971). Because the eccentricities do not meet this significance threshold and because the other parameters agree across all four scenarios within 1σ,

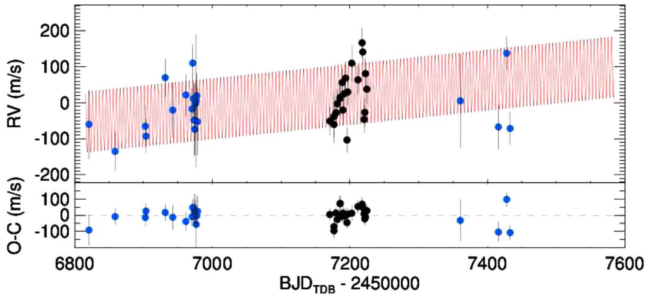

Figure 8. Adopted best-fit radial velocity of KELT-12, including slope. The 0.16 ± 0.065 m s^{-1} day^{-1} slope is inconsistent with zero at the 2.4σ level.

Table 5
Transit Times for KELT-12b

Epoch	T_C (BJD$_{TDB}$)	σ_{T_C} (s)	O–C (s)	O–C (σ_{T_C})	Telescope
−41	2,456,877.366443	354	213.23	0.60	CROW
−31	2,456,927.678294	275	−163.86	−0.59	PvdKO
−31	2,456,927.686765	398	568.03	1.42	Kutztown
−31	2,456,927.674336	499	−505.83	−1.01	Kutztown
−31	2,456,927.677586	334	−225.03	−0.67	PvdKO
7	2,457,118.881931	171	10.50	0.06	KeplerCam
25	2,457,209.450076	253	−79.61	−0.31	Salerno
25	2,457,209.454940	231	340.64	1.47	ZRO
26	2,457,214.484444	340	157.68	0.46	Salerno
26	2,457,214.485726	185	268.45	1.45	ZRO
27	2,457,219.513254	236	−85.24	−0.36	ZRO
28	2,457,224.535085	278	−931.14	−3.34	ZRO
33	2,457,249.702566	216	−121.29	−0.56	PvdKO
34	2,457,254.738131	264	219.42	0.83	MVRC
34	2,457,254.735365	163	−19.56	−0.12	MVRC

we adopt the YY circular global fit for our analyses in this paper.

We note that all four cases exhibit a best-fit RV slope that is inconsistent with zero at the $\sim 2.4\sigma$ level. While we do not claim a strong detection of an RV slope given this low significance, we note that long-term RV monitoring would determine whether or not the RV slope is physical and, if so, whether it is due to a massive outer companion. Figure 8 shows the RV slope for the adopted best-fit model.

We searched for TTVs in the system by allowing the transit times for each follow-up light curve to vary. The ephemeris is constrained by the RV data and a prior imposed from the KELT-North discovery light curve and the follow-up photometry. The transit times are listed in Table 5 and Figure 9. Relative to the best-fit linear ephemeris, we find only one $\sim 3\sigma$ TTV, on epoch 25, but a $\sim 1.2\sigma$ deviation from a different observatory during the same epoch suggests that this TTV is likely spurious. Hence, we do not claim evidence for TTVs in the KELT-12 system.

Finally, we report a high-precision ephemeris for the KELT-12 system. The time of inferior conjunction in BJD$_{TDB}$ is $T_0 = 2457083.660459 \pm 0.00089410119$, and the period is $P = 5.0316216 \pm 0.000031681325$ days. These are also included in Table 4.

5. False-positive Analysis

We perform several analyses to exclude possible false-positive scenarios. First, we find that the depths found in all our follow-up light curves are consistent with each other, even across different photometric filters. Moreover, the follow-up observations are well modeled by a dark companion occulting a star, and the limb-darkening effects on the light curves from the host star are consistent with the $T_{\rm eff}$ and $\log g_\star$ determined from the spectrum. We can therefore rule out a blended EB scenario in which the blended stars have significantly different colors, as such a blend would effect detectable differences in the measured depths across our photometric filters.

We also investigate the possibility that the RV variations are caused by stellar activity or a nearby, unresolved eclipsing binary; in these cases, spectral line asymmetries will induce BS variations that correlate with RV. We calculate the APF BS measurements as described in Section 5.2 of Fulton et al. (2015), and we follow Torres et al. (2007) to calculate the TRES BS measurements. Analyzing both the APF and TRES measurements, we calculate a Spearman rank correlation coefficient of -0.26 ($p = 0.0973$), which does not indicate a significant correlation between BS and RV. The BS measurements and uncertainties are listed in Table 3 and are plotted versus RV in Figure 10.

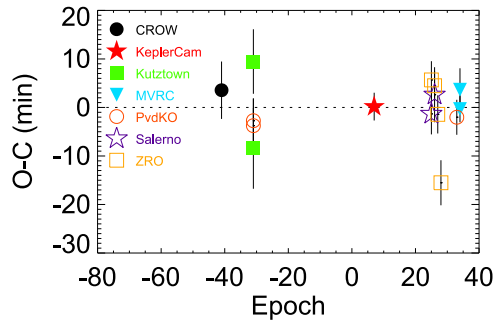

Figure 9. Transit time residuals for KELT-12b using our final global fit ephemeris. The times are listed in Table 5, and the observatory abbreviations are given in Section 2.2.

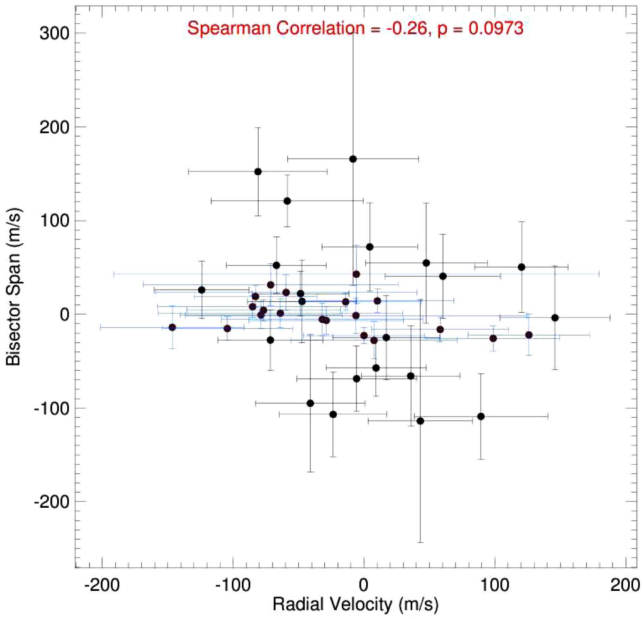

Figure 10. BS measurements from APF (black) and TRES (blue) showing no coherent trend with RV.

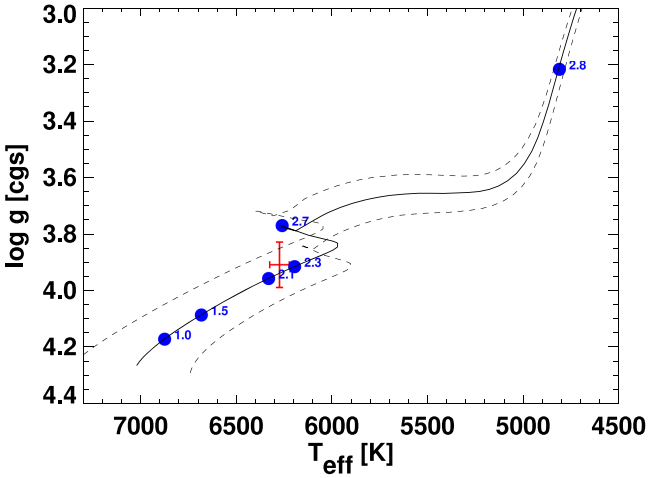

Figure 11. Theoretical H-R diagrams based on the YY stellar evolution models (Demarque et al. 2004). The red cross shows the values of and 1σ uncertainties on $T_{\rm eff}$ and $\log g_\star$ from the adopted global fit in Table 4. The black curve shows the best-fit evolutionary track, while the dashed lines show evolutionary tracks for the 1σ uncertainties on [Fe/H] and M_*. The blue filled circles denote the $\log g_\star$ and $T_{\rm eff}$ for KELT-12 at the listed ages (in Gyr).

Additionally, our *R*- and *I*-band DSSI speckle imaging and K_s-band NIRC2 AO enable us to exclude stellar companions to KELT-12 down to a 9 mag contrast at $1''$ separation at 5σ significance. Figure 5 shows the DSSI *R*- and *I*-band contrast curves, and Figure 6 shows the NIRC2 contrast curve.

6. Evolutionary Analysis

6.1. Stellar Models and Age

To estimate KELT-12's age, we use the $T_{\rm eff}$, $\log g_\star$, M_*, and [Fe/H] values from the adopted global fit (see Table 4), along with evolutionary tracks from the YY stellar models (Demarque et al. 2004). We assume uniform priors on $T_{\rm eff}$, $\log g_\star$, and [Fe/H], resulting in a nonuniform prior on the stellar age. Figure 11 shows the best-fit theoretical H-R diagram for KELT-12, along with evolutionary tracks that correspond to the 1σ uncertainties in $T_{\rm eff}$ and M_*. We infer that KELT-12 is 2.2 ± 0.1 Gyr old (Table 1), approaching the end of its main-sequence lifetime but not yet a subgiant; we note that this age is model dependent.

6.2. Insolation Evolution

Demory & Seager (2011) found that planets receiving more than 2×10^8 erg s^{-1} cm^{-2} insolation from their host stars will have inflated radii compared to planets receiving insolation below this threshold. As listed in Table 4, KELT-12b receives over 10 times as much flux, with an insolation of $2.38^{+0.32}_{-0.29} \times 10^9$ erg s^{-1} cm^{-2}. Along with a density $\rho_{\rm P} = 0.209^{+0.071}_{-0.053}$ g cm^{-3} and a mass $M_{\rm P} = 0.95 \pm 0.14 M_{\rm Jup}$, KELT-12b is an inflated hot Jupiter that follows the insolation–inflation trend of Demory & Seager (2011). It is worth investigating KELT-12b's insolation history to determine whether or not its incident flux always exceeded the Demory & Seager (2011) threshold. An understanding of KELT-12b's insolation evolution enables us to examine the timescales of planetary inflation mechanisms (e.g., Assef et al. 2009; Spiegel & Madhusudhan 2012).

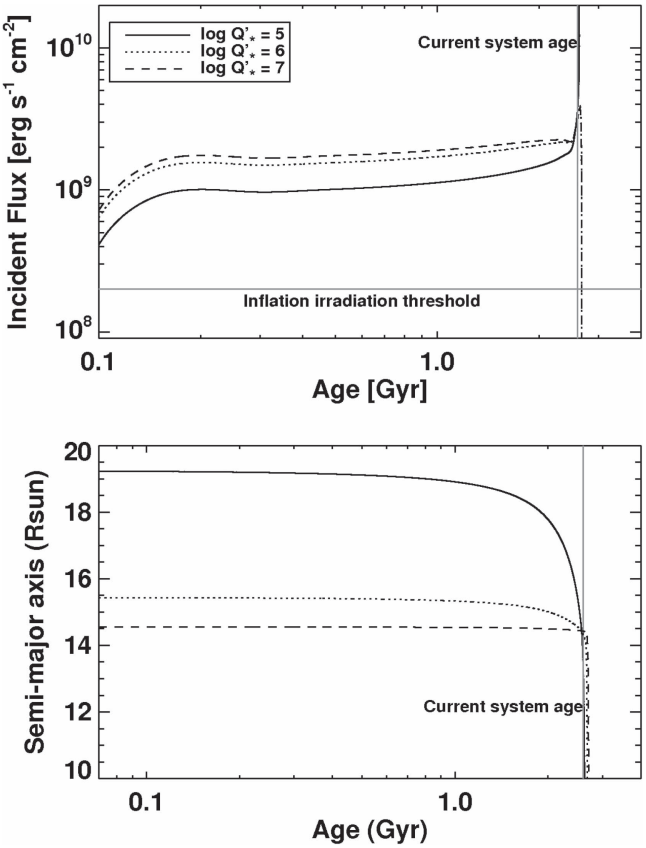

Figure 12. Insolation (top) and semimajor-axis (bottom) evolution of KELT-12b for stellar tidal quality factors $Q_* = 10^5$ (solid), 10^6 (dotted), and 10^7 (dashed).

To infer KELT-12b's insolation history, we simulate the evolution of the KELT-12 system. We impose the adopted global fit parameters (see Table 4) as the present-day boundary conditions. We assume solid-body rotation for KELT-12 and that tidal torques exerted by the planet are the only physical influence on the stellar rotation. We test three stellar tidal quality factors Q_*: $\log Q_* = 5$, 6, and 7. Figure 12 shows the results of our simulation. The top panel shows that KELT-12b's incident flux has exceeded the Demory & Seager (2011) threshold throughout KELT-12's main-sequence lifetime, despite its large orbital separation (bottom panel); as a result, KELT-12b has always received an amount of stellar insolation that is greater than the boundary suggested by Demory & Seager (2011) for inflated hot Jupiters. Moreover, the insolation is insensitive to our choice of Q_* for the system parameters that we have adopted.

7. Discussion

7.1. Trends in Radius Inflation

As mentioned in Section 6.2, Demory & Seager (2011) found that planets irradiated at levels above $F = 2 \times 10^8$ erg s^{-1} cm^{-2} are inflated relative to less irradiated planets; additionally, Weiss et al. (2013) found that $R_{\rm P} \propto F^{0.094}$ for planets with $M_{\rm P} > 150\,M_\oplus$, whereas $R_{\rm P} \propto F^{-0.03}$ for less massive planets. Since all transiting gas giant planets discovered by KELT (along with the brown dwarf KELT-1b) receive stellar flux in excess of this amount, a significant fraction of KELT planets exhibit inflated

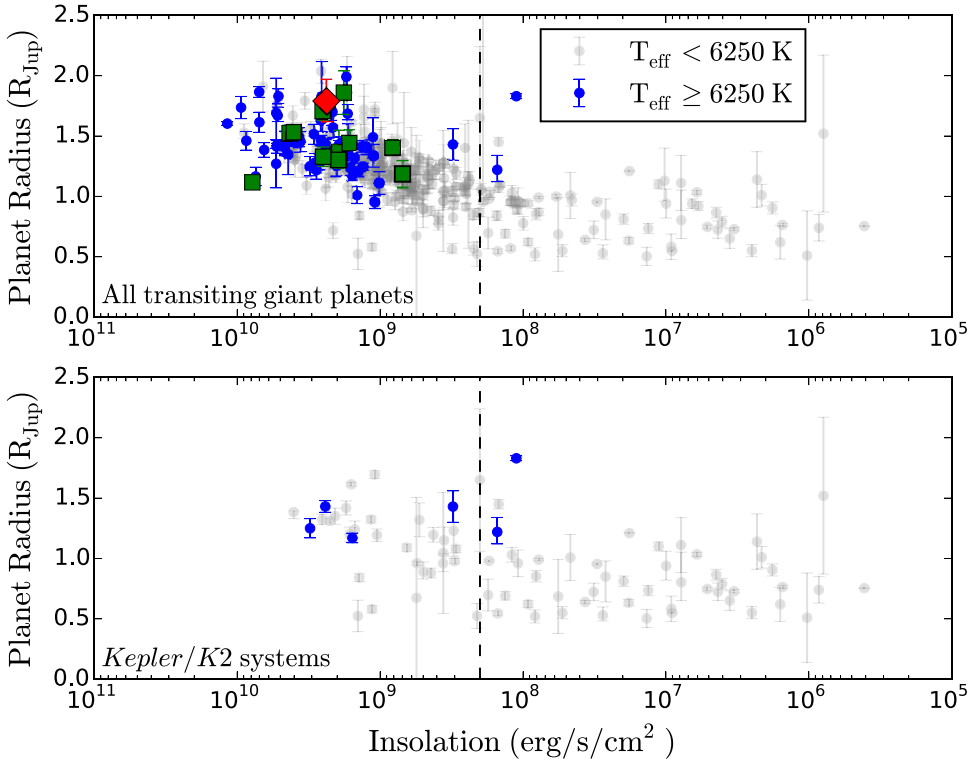

Figure 13. Top: inferred planet radius as a function of calculated incident flux for transiting giant ($R_P \geqslant 0.5R_{Jup}$) planets, with planets around hot ($T_{eff} \geqslant 6250$ K) stars in blue and planets around cooler stars in gray. The vertical dashed line marks the 2×10^8 erg s^{-1} cm^{-2} insolation threshold above which giant planets tend to be inflated (Demory & Seager 2011). The red diamond denotes KELT-12b, while the green squares denote the other KELT discoveries. Bottom: same as the top panel, but restricted to transiting planets discovered by the *Kepler* and *K2* missions.

radii. Since most KELT planet hosts are also hotter than the Kraft break at $T_{eff} = 6250$ K (Kraft 1967), we investigate associations among planet radius, insolation, and host star effective temperature to check whether or not those system parameters are typical of transiting hot Jupiters.

Figure 13 shows the planet radius as a function of insolation for transiting planets in the Extrasolar Planet Encyclopedia[42] (Schneider et al. 2011). To within the uncertainties, KELT-12b is one of the largest—if not the largest—transiting hot Jupiters known. In this analysis, we restrict ourselves to the KELT-12 system (red diamond) plus the 339 transiting systems with listed host radii, companion radii $R_P \geqslant 0.5R_{Jup}$, semimajor axes, and host effective temperatures.

As the top panel of Figure 13 shows, transit surveys have found giant planets with insolation below 2×10^8 erg s^{-1} cm^{-2}, but few of those have radii above $1R_{Jup}$. Above this threshold, the radii of known giant planets increase; above 10^9 erg s^{-1} cm^{-2}, the overwhelming majority of planets have $R_P > R_{Jup}$, with only four planets having smaller radii.

To examine whether or not this distribution changes with stellar effective temperature, we divided the sample into transiting giant planets around hot stars (blue filled circles) and cool stars (gray filled circles), using the Kraft break ($T_{eff} = 6250$ K) as the partition. We chose this effective temperature for its physical significance: stars above this temperature have largely radiative envelopes, with very thin or even absent convective envelopes, whereas stars cooler than 6250 K have increasingly larger convective envelopes (Kraft 1967). As a result, stars cooler than the Kraft break have magnetic fields that cause them to spin down with time, whereas hotter stars largely retain their primordial spin rates. While both samples show radius inflation above the Demory & Seager (2011) threshold, none of the 64 planets in our "hot" sample have radii below $1R_{Jup}$, and only two receive less than 2×10^8 erg s^{-1} cm^{-2} incident flux.

Figure 14 shows planet radius as a function of period for the same two populations of giant planets. For giant planets around cool stars, the planet radius decreases with increasing orbital period (hence decreasing incident flux). However, all but a couple of known giant planets around hot stars are on short-period orbits; only three systems orbit on $P > 10$ day periods, and all three have radii that are distinctly larger than the radii of the giant planets around cool stars at comparable periods.

We note that the paucity of giant planets with low insolation around hot stars is most likely a selection effect. The bottom panel of Figure 13 shows the planet radius versus insolation for the subsample of 77 giant planets discovered by *Kepler* and *K2*. This subsample includes the bulk of systems below the Demory & Seager (2011) threshold. Only six of the *Kepler* systems orbit hot stars, including the two receiving low incident flux. *Kepler* avoided searching for planets around hot stars (Batalha et al. 2010), which explains the dearth of such systems. Conversely, ground-based transit surveys are biased toward discovering large planets on short orbits (Beatty & Gaudi 2008) and thus are biased toward planets receiving high amounts of radiation from their hosts.

From our available data, we cannot support the hypothesis that giant planets around hotter stars tend to be more inflated

[42] http://www.exoplanet.eu, accessed 2016 July 17.

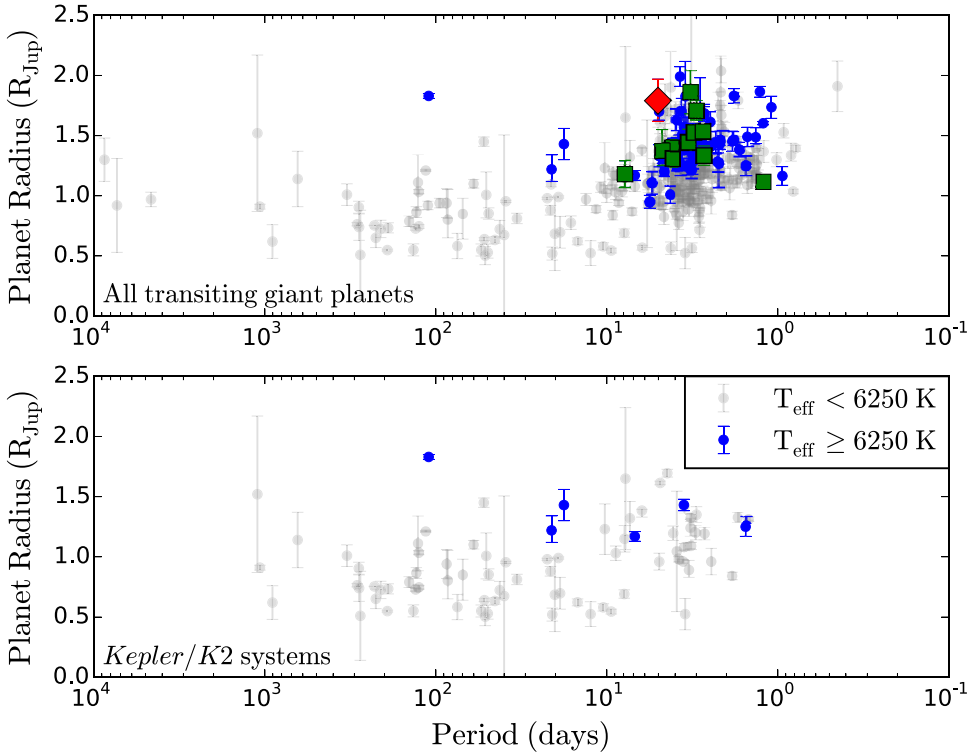

Figure 14. Top: inferred planet radius as a function of orbital period for transiting giant ($R_P \geqslant 0.5 R_{Jup}$) planets, with planets around hot ($T_{eff} \geqslant 6250$ K) stars in blue and planets around cooler stars in gray. The red diamond denotes KELT-12b, while the green squares denote the other KELT discoveries. Bottom: same as the top panel, but restricted to transiting planets discovered by the *Kepler* and *K2* missions.

than giant planets around cooler stars until the selection effects of ground- and space-based surveys are taken into account. The *TESS* target sample includes hot stars and will recover some longer-period systems (Sullivan et al. 2015), and this will be complemented by ground-based transit surveys' increasing sensitivity to longer-period transiting systems (due to the increasing baseline of observations). In the coming years, we will extend the sample of hot Jupiters around hot stars to longer periods (and thus lower insolations), putting us in a better position to investigate any differences in giant planet inflation caused by the stellar effective temperature.

8. Conclusion

We announce the discovery of KELT-12b, an inflated hot Jupiter on a 5.03-day period around a mildly evolved star. KELT-12 appears to be a single-star system, as AO imaging has revealed no companions beyond $1''$ within 9 mag in apparent brightness. With a mass of $0.95 \pm 0.14 M_{Jup}$ and a radius of $1.78^{+0.17}_{-0.16} R_{Jup}$, KELT-12b is one of the most inflated hot Jupiters known, despite its relatively long orbital period.

The majority of giant planets transiting hot ($T_{eff} \geqslant 6250$ K) stars have radii exceeding $1 R_{Jup}$ and receive stellar flux exceeding 2×10^8 erg s^{-1} cm^{-2}—the threshold above which giant planets appear inflated, as found by Demory & Seager (2011). However, the lack of giant planets around hot stars on long-period orbits (and therefore receiving less stellar radiation) is likely due to selection biases in both ground- and space-based transit surveys. Determining whether giant planets around hot stars are systematically more inflated than giant planets around cooler stars hinges on both the inclusion of hot stars in the *TESS* survey sample and the longevity of ongoing ground-based transit surveys such as HAT, KELT, and SuperWASP.

The authors thank the anonymous reviewer and scientific editor for helpful suggestions regarding both form and content.

Work by B.S.G. and D.J.S. was partially supported by NSF CAREER Grant AST-1056524. B.J.F. notes that this material is based on work supported by the National Science Foundation Graduate Research Fellowship under grant no. 2014184874. Any opinion, findings, and conclusions or recommendations expressed in this material are those of the authors(s) and do not necessarily reflect the views of the National Science Foundation. K.K.M. acknowledges the purchase of SDSS filters for Whitin Observatory by the Theodore Dunham, Jr., Grant of the Fund for Astronomical Research. The NIRC2 AO data in this work were obtained at the W. M. Keck Observatory, which was financed by the W. M. Keck Foundation and is operated as a scientific partnership between the California Institute of Technology, the University of California, and NASA. K.P. acknowledges support from NASA grant NNX13AQ62G.

DSSI data presented herein were obtained at the WIYN Observatory from telescope time allocated to NN-EXPLORE through the scientific partnership of the National Aeronautics and Space Administration, the National Science Foundation, and the National Optical Astronomy Observatory. This work was supported by a NASA WIYN PI Data Award, administered by the NASA Exoplanet Science Institute. We gratefully acknowledge the help of the DSSI team in observing KELT-12 and reducing the DSSI data.

This work has made use of NASA's Astrophysics Data System, the Extrasolar Planet Encyclopedia at http://exoplanet.eu (Schneider et al. 2011), the SIMBAD database operated at CDS, Strasbourg, France, and the VizieR catalog access tool, CDS, Strasbourg, France (Ochsenbein et al. 2000).

This publication makes use of data products from the *Wide-field Infrared Survey Explorer*, which is a joint project of the University of California, Los Angeles; the Jet Propulsion Laboratory/California Institute of Technology, which is funded by the National Aeronautics and Space Administration; the Two Micron All Sky Survey, which is a joint project of the University of Massachusetts and the Infrared Processing and Analysis Center/California Institute of Technology, funded by the National Aeronautics and Space Administration and the National Science Foundation; and the American Association of Variable Star Observers (AAVSO) Photometric All-Sky Survey (APASS), whose funding is provided by the Robert Martin Ayers Sciences Fund and the AAVSO Endowment (https://www.aavso.org/aavso-photometric-all-sky-survey-data-release-1).

References

Alard, C. 2000, A&AS, 144, 363
Alard, C., & Lupton, R. H. 1998, ApJ, 503, 325
Assef, R. J., Gaudi, B. S., & Stanek, K. Z. 2009, ApJ, 701, 1616
Bakos, G., Noyes, R. W., Kovács, G., et al. 2004, PASP, 116, 266
Batalha, N. M., Borucki, W. J., Koch, D. G., et al. 2010, ApJL, 713, L109
Beatty, T. G., Collins, K. A., Fortney, J., et al. 2014, ApJ, 783, 112
Beatty, T. G., & Gaudi, B. S. 2008, ApJ, 686, 1302
Bensby, T., Feltzing, S., & Lundström, I. 2003, A&A, 410, 527
Borucki, W. J., Koch, D., Basri, G., et al. 2010, Sci, 327, 977
Brown, T. M. 2003, ApJL, 593, L125
Buchhave, L. A., Bakos, G. Á., Hartman, J. D., et al. 2010, ApJ, 720, 1118
Buchhave, L. A., Latham, D. W., Johansen, A., et al. 2012, Natur, 486, 375
Coşkunoğlu, B., Ak, S., Bilir, S., et al. 2011, MNRAS, 412, 1237
Collier Cameron, A., Wilson, D. M., West, R. G., et al. 2007, MNRAS, 380, 1230
Collins, K., & Kielkopf, J. 2013, AstroImageJ: ImageJ for Astronomy, Astrophysics Source Code Library, ascl:1309.001
Collins, K. A., Eastman, J. D., Beatty, T. G., et al. 2014, AJ, 147, 39
Collins, K. A., Kielkopf, J. F., & Stassun, K. G. 2016, arXiv:1601.02622
Cutri, R. M., Skrutskie, M. F., van Dyk, S., et al. 2003, yCat, 2246, 0
Demarque, P., Woo, J.-H., Kim, Y.-C., & Yi, S. K. 2004, ApJS, 155, 667
Demory, B.-O., & Seager, S. 2011, ApJS, 197, 12
Eastman, J., Gaudi, B. S., & Agol, E. 2013, PASP, 125, 83
Eastman, J. D., Beatty, T. G., Siverd, R. J., et al. 2016, AJ, 151, 45
Faedi, F., Gómez Maqueo Chew, Y., Pollacco, D., et al. 2016, arXiv:1608.04225
Fressin, F., Guillot, T., Morello, V., & Pont, F. 2007, A&A, 475, 729
Fulton, B. J., Weiss, L. M., Sinukoff, E., et al. 2015, ApJ, 805, 175
Gaudi, B. S. 2005, ApJL, 628, L73
Gould, A., & Morgan, C. W. 2003, ApJ, 585, 1056
Hartman, J. 2012, VARTOOLS: Light Curve Analysis Program, Astrophysics Source Code Library, ascl:1208.016
Hauschildt, P. H., Allard, F., Ferguson, J., Baron, E., & Alexander, D. R. 1999, ApJ, 525, 871
Henden, A. A., Levine, S., Terrell, D., & Welch, D. L. 2015, AAS Meeting 225 Abstracts, #336.16
Høg, E., Fabricius, C., Makarov, V. V., et al. 2000, A&A, 355, L27
Horch, E. P., Gomez, S. C., Sherry, W. H., et al. 2011, AJ, 141, 45
Horch, E. P., Veillette, D. R., Baena Gallé, R., et al. 2009, AJ, 137, 5057
Howell, S. B., Everett, M. E., Sherry, W., Horch, E., & Ciardi, D. R. 2011, AJ, 142, 19
Howell, S. B., Sobeck, C., Haas, M., et al. 2014, PASP, 126, 398
Jensen, E. 2013, Tapir: A web interface for transit/eclipse observability, Astrophysics Source Code Library, ascl:1306.007
Kovács, G., Bakos, G., & Noyes, R. W. 2005, MNRAS, 356, 557
Kovács, G., Zucker, S., & Mazeh, T. 2002, A&A, 391, 369
Kraft, R. P. 1967, ApJ, 150, 551
Lucy, L. B., & Sweeney, M. A. 1971, AJ, 76, 544
Martin, D. C., Fanson, J., Schiminovich, D., et al. 2005, ApJL, 619, L1
Ochsenbein, F., Bauer, P., & Marcout, J. 2000, A&AS, 143, 23
Pepper, J., & Gaudi, B. S. 2005, ApJ, 631, 581
Pepper, J., Gould, A., & Depoy, D. L. 2003, AcA, 53, 213
Pepper, J., Kuhn, R. B., Siverd, R., James, D., & Stassun, K. 2012, PASP, 124, 230
Pepper, J., Pogge, R. W., DePoy, D. L., et al. 2007, PASP, 119, 923
Pepper, J., Rodriguez, J. E., Collins, K. A., et al. 2016, arXiv:1607.01755
Petigura, E. A. 2015, PhD thesis, Univ. California
Pollacco, D. L., Skillen, I., Collier Cameron, A., et al. 2006, PASP, 118, 1407
Pont, F., Zucker, S., & Queloz, D. 2006, MNRAS, 373, 231
Richmond, M. W., Droege, T. F., Gombert, G., et al. 2000, PASP, 112, 397
Ricker, G. R., Winn, J. N., Vanderspek, R., et al. 2015, JATIS, 1, 014003
Rouan, D., Baglin, A., Copet, E., et al. 1998, EM&P, 81, 79
Schneider, J., Dedieu, C., Le Sidaner, P., Savalle, R., & Zolotukhin, I. 2011, A&A, 532, A79
Seager, S., & Deming, D. 2010, ARA&A, 48, 631
Sing, D. K., Fortney, J. J., Nikolov, N., et al. 2016, Natur, 529, 59
Siverd, R. J., Beatty, T. G., Pepper, J., et al. 2012, ApJ, 761, 123
Skrutskie, M. F., Cutri, R. M., Stiening, R., et al. 2006, AJ, 131, 1163
Spiegel, D. S., & Madhusudhan, N. 2012, ApJ, 756, 132
Stetson, P. B. 1987, PASP, 99, 191
Sullivan, P. W., Winn, J. N., Berta-Thompson, Z. K., et al. 2015, ApJ, 809, 77
Torres, G., Andersen, J., & Giménez, A. 2010, A&ARv, 18, 67
Torres, G., Konacki, M., Sasselov, D. D., & Jha, S. 2005, ApJ, 619, 558
Torres, G., Bakos, G. Á., Kovács, G., et al. 2007, ApJL, 666, L121
Weiss, L. M., Marcy, G. W., Rowe, J. F., et al. 2013, ApJ, 768, 14
Wright, E. L., Eisenhardt, P. R. M., Mainzer, A. K., et al. 2010, AJ, 140, 1868
Zacharias, N., Monet, D. G., Levine, S. E., et al. 2004, AAS Meeting 205 Abstracts, #48.15
Zhou, G., Rodriguez, J. E., Collins, K. A., et al. 2016, arXiv:1607.03512